

Winds of Change: *XRISM* Resolve X-ray spectroscopy of NGC 4051

JAMES N. REEVES,^{1,2} SHOJI OGAWA,³ TRACEY J. TURNER,⁴ VALENTINA BRAITO,^{5,6,1} SATOSHI YAMADA,^{7,8} STEVEN B. KRAEMER,¹ HIROFUMI NODA,⁸ ANNA TRINDADE FALCÃO,⁹ MARTIN ELVIS,¹⁰ AND GIUSEPPINA FABBIANO¹⁰

¹*Institute for Astrophysics and Computational Sciences, Department of Physics, The Catholic University of America, Washington, DC 20064, USA*

²*INAF, Osservatorio Astronomico di Brera, Via Bianchi 46, I-23807 Merate (LC), Italy*

³*Institute of Space and Astronautical Science (ISAS), Japan Aerospace Exploration Agency (JAXA), Sagamihara, Kanagawa 252-5210, Japan*

⁴*Eureka Scientific, Inc., 2452 Delmer Street Suite 100, Oakland, CA 94602-3017, USA*

⁵*INAF, Osservatorio Astronomico di Brera, Via Brera 20, I-20121 Milano, Italy*

⁶*Dipartimento di Fisica, Università di Trento, Via Sommarive 14, Trento 38123, Italy*

⁷*The Frontier Research Institute for Interdisciplinary Sciences, Tohoku University, Aramaki, Aoba-ku, Sendai, Miyagi 980-8578, Japan*

⁸*Astronomical Institute, Tohoku University, Aramaki, Aoba-ku, Sendai, Miyagi 980-8578, Japan*

⁹*NASA Goddard Space Flight Center, Code 662, Greenbelt, MD 20771, USA*

¹⁰*Harvard-Smithsonian Center for Astrophysics, 60 Garden St., Cambridge, MA 02138, USA*

ABSTRACT

NGC 4051 is a nearby (16.7 Mpc), Narrow Line Seyfert 1 galaxy (NLS1), which has a low black hole mass of $10^6 M_{\odot}$. It is also known for its rapid X-ray variability, on timescales of kilo-seconds and has a complex, multi component wind in both the soft X-ray and Fe K bands. Here we present the first high resolution *XRISM* Resolve spectrum of NGC 4051, which was captured in a historically bright state for a 150 ks exposure. *XRISM* resolves two blue-shifted Fe K shell absorption troughs in the mean spectrum, which can be ascribed to H-like iron and arises from two outflow components with outflow velocities of 0.025c and 0.04c. A time dependent spectral analysis shows that the iron K absorption is variable on timescales of less than a day, increasing in velocity over the duration of the observation. The velocity changes may be explained either by the passage of two separate transiting absorbers, of different velocities, or by a single accelerating outflow of approximately constant column density. In the latter case, the wind acceleration is likely to be too large to be caused by radiation pressure and instead magnetic driving is favored to accelerate the wind up to 0.04c. The outflow can originate from an accretion disk wind, whose kinetic power is sub-Eddington in contrast to recent examples of winds from powerful, luminous quasars observed by *XRISM*.

Keywords: Galaxies (573) — High Energy astrophysics (739) — X-ray active galactic nuclei (2035)

1. INTRODUCTION

X-ray outflows are common in type I Active Galactic Nuclei (AGN). In Seyfert 1s, warm absorbers are observed in soft X-ray grating spectra, originating from low velocity outflows at typically hundreds to a few thousand kilometers per second (D. M. Crenshaw et al. 2003; A. J. Blustin et al. 2005; S. Laha et al. 2021). In the iron K band, CCD resolution spectra often reveal absorption from K-shell lines of He and H-like iron (G. Chartas et al. 2003, 2002; K. A. Pounds et al. 2003; J. N. Reeves et al. 2003; F. Tombesi et al. 2010; J. Gofford et al. 2013; E. Nardini et al. 2015; G. A. Matzeu et al. 2023; S. Yamada et al. 2024; M. Laurenti et al. 2025). This gas is of higher ionization than the warm absorbers and their velocities can reach 0.1c or higher in the so-called Ultra Fast Outflows (UFOs), indicating that they originate

from matter ejected close to the super-massive black hole (F. Tombesi et al. 2013). As a result of their enhanced energetics, UFOs can play an important role in black-hole and host galaxy co-evolution (A. R. King 2003, 2010; P. F. Hopkins et al. 2016).

The Resolve calorimeter onboard *XRISM* provides a Full Width at Half Maximum (FWHM) spectral resolution of ~ 4.5 eV (M. Tashiro et al. 2025). Resolve thus provides precise measurements of highly ionized outflows measured in the iron K band, as is seen during initial observations of AGN; e.g. PDS 456 (XRISM Collaboration et al. 2025), NGC 3783 (M. Mehdipour et al. 2025) IRAS 05189–2524 (H. Noda et al. 2025), PG 1211+143 (M. Mizumoto et al. 2026), NGC 4151 (X. Xiang et al. 2025), NGC 3516 (A. Juráňová et al. 2025), MCG –6–30–15 (L. W. Brenneman et al. 2025) and NGC 1365 (F. Zaidouni et al. 2026). These observations have revealed outflow velocities ranging from just a

Table 1. Observation log of the 2025 NGC 4051 campaign

Instrument	Obs. ID	Start Date	End Date	Exposure ^a	Count Rate ^b
XRISM Resolve	201066010	2025-05-16 18:01:30	2025-05-20 06:28:10	134	0.437 ± 0.002
XRISM Xtend	201065010	2025-05-16 17:54:41	2025-05-20 06:59:27	157	6.798 ± 0.007
NuSTAR FPMA+B	61101003002	2025-05-15 16:24:51	2025-05-19 05:41:06	316	1.301 ± 0.003
XMM-Newton 1 EPIC-pn	0960150201	2025-05-15 21:37:36	2025-05-17 05:53:32	80.5	34.10 ± 0.02
XMM-Newton 2 EPIC-pn	0960150301	2025-05-17 16:39:34	2025-05-19 05:13:22	85	35.28 ± 0.02

^aNet exposure time in units of ks.

^bObserved background-subtracted count rate in units of ct s^{-1} . The *NuSTAR* rate is for FPMA+B combined.

few hundred kilometers per second up to a substantial fraction of the speed of light, over a range of radial distances and often with complex and clumpy structures.

Not only can Resolve precisely measure the outflow kinematics, it can also probe the outflow variability on timescales of a day or less, potentially providing insight into the wind acceleration mechanisms. Notably, the *XRISM* observation of the Seyfert galaxy NGC 3783 captured the emergence of an ultra fast outflow, which appears to accelerate from $0.05c$ to $0.30c$, a rate at which [L. Gu et al. \(2025\)](#) infer to be too large to be due to radiation pressure, favoring magnetic hydrodynamical (MHD) driving mechanisms ([R. D. Blandford & D. G. Payne 1982](#); [K. Fukumura et al. 2010](#)).

The subject of this paper is NGC 4051, a bright, nearby (16.6 Mpc, $z = 0.002336$; [W. Yuan et al. 2021](#)) Narrow Line Seyfert 1 AGN with bolometric luminosity $\sim 10^{43.4} \text{erg s}^{-1}$ ([A. J. Blustin et al. 2005](#)). Measurements of the lag time between variations in the continuum and $\text{H}\beta$ emission line lead to a measured radius for the optical broad line region (BLR) of $R_{\text{BLR}} \approx 2$ light-days and a black hole mass of $M_{\text{BH}} \approx 10^6 M_{\odot}$ ([K. D. Denney et al. 2009](#); [M. M. Fausnaugh et al. 2017](#)), with typical 0.3 dex uncertainties.

NGC 4051 has a strong Fe $\text{K}\alpha$ line and a well-studied multi-zoned X-ray absorber, originating from a variable nuclear wind ([K. A. Pounds et al. 2004](#); [Y. Krongold et al. 2007](#); [R. Serafinelli et al. 2025](#)). It also shows pronounced iron K shell absorption, as revealed by earlier CCD resolution spectra ([A. P. Lobban et al. 2011](#); [K. A. Pounds & S. Vaughan 2012](#)), which are blue-shifted by typically $5000 - 7000 \text{ km s}^{-1}$. A further faster UFO component can also be present in some observations, reaching velocities of up to $\sim 0.12c$ ([F. Tombesi et al. 2010](#)) and which appear to be variable on a ~ 2 day timescale ([K. A. Pounds & S. Vaughan \(2012\)](#)).

A *XRISM* observation of NGC 4051 was conducted in May 2025, supported by *NuSTAR* and *XMM-Newton*, as is summarized in Table 1 and illustrated in Figure 1 for each instru-

ment. The AGN shows a high level of variability throughout the campaign. Here we present the signature and variability of the iron K band absorber at high resolution. Section 2 describes the observations. Section 3 presents the mean spectral analysis, providing a characterization of the absorption line profiles measured by Resolve. These appear to originate from mini-UFOs, with outflow velocities from $0.02 - 0.04c$. Section 4 describes the time variable iron K absorption, where an increase in outflow velocity occurs during the *XRISM* exposure. Section 5 interprets this in terms of either transiting material or an accelerating outflow. Future work will present the detailed analysis of the iron K band emission profiles and the soft X-ray grating spectra.

2. DATA ANALYSIS

2.1. XRISM

A *XRISM* observation was conducted for NGC 4051 with a total duration of ~ 300 ks. Data were screened to exclude periods during Earth occultation and passages through the South Atlantic Anomaly (SAA). In addition, times within 4300 s of the initiation of the cryogenic cooler recycling, and visibility of the Earth’s sunlit limb were also excluded. After event screening the effective exposure time for Resolve was 134 ks and 157 ks for Xtend.

For the Resolve spectra and responses, only the Hp (High-resolution Primary) events were utilized and low resolution secondary events (L_S pseudo events) were excluded from the analysis. The data reduction used pipeline software version 03.01.014.010 with calibration database CALDB 20241115. In addition to the calibration pixel, pixel 27 is excluded from analysis as it exhibits random gain spikes of unknown origin. The on-board Fe-55 calibration pixel confirms an in-flight Resolve resolution of $4.55 \pm 0.05 \text{ eV}$ (FWHM), with an energy scale uncertainty of $\pm 1 \text{ eV}$.

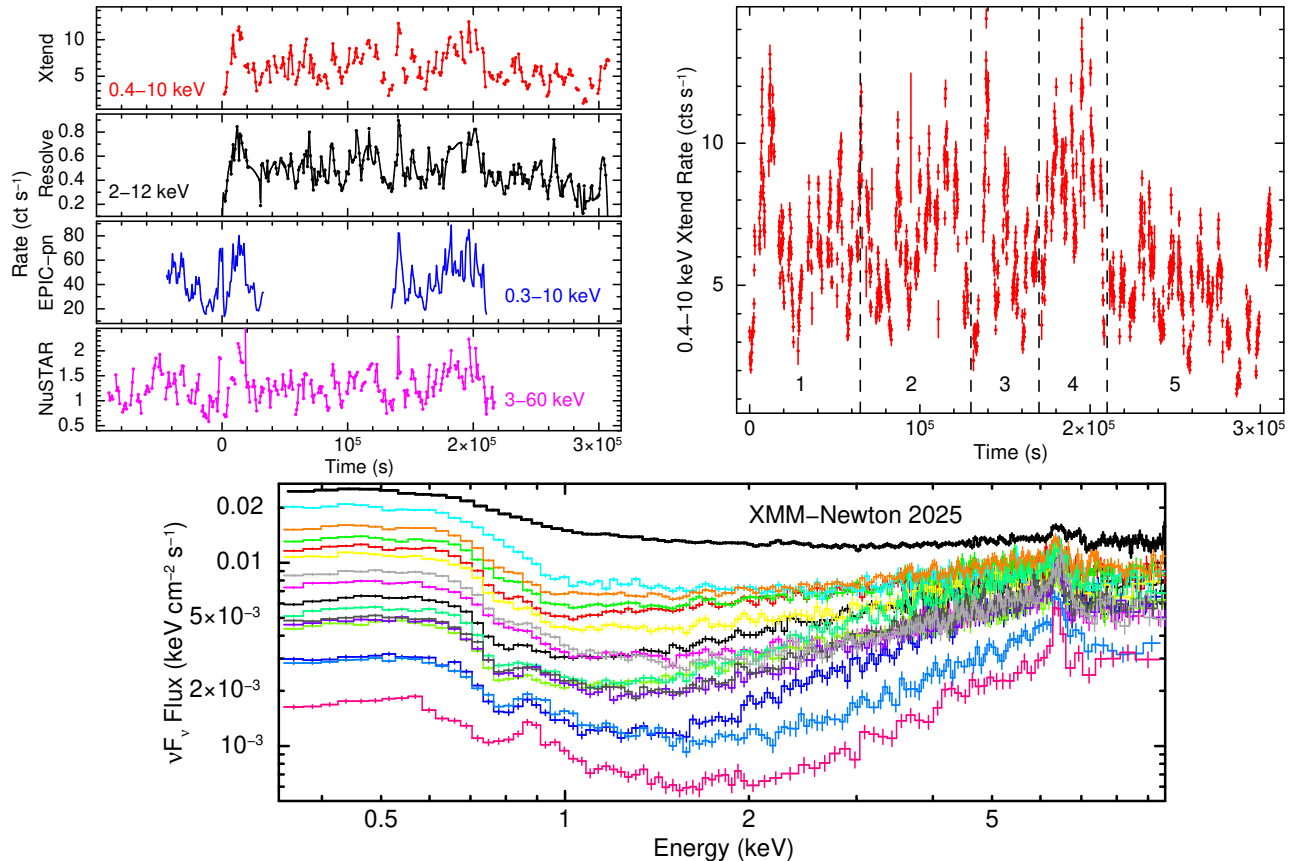


Figure 1. The X-ray variability of NGC 4051. The upper left panels show the 2025 light-curves (top to bottom) from Xtend, Resolve, EPIC-pn and NuSTAR. Time is relative to the start time of the *XRISM* Resolve exposure. The right-hand plot shows a zoom in of the 0.4–10 keV Xtend lightcurve, with finer time binning of 128 s per bin. Multiple short timescale kilo-second flares are present. The vertical dashed lines denote the time intervals used for the time sliced spectral analysis. The lower panel highlights the long term spectral variability, where the 2025 *XMM-Newton* EPIC-pn spectrum (bold black points) is observed at a historical high flux compared to the 15 EPIC-pn spectra taken in 2009.

A stacked Non X-ray Background (NXB) spectrum¹¹ was generated and found to be negligible compared to the AGN; the total Resolve count-rate is $0.442 \pm 0.002 \text{ ct s}^{-1}$ from 2–10 keV, of which the NXB contribution is only 1%. The mean Resolve spectrum was binned to 2 eV per bin for spectral fitting to over-sample the FWHM resolution and was also re-sampled to 10 eV and 20 eV per bin for plotting purposes. For the time sliced analysis, the coarser binning is used.

An Xtend CCD spectrum was extracted from a circular source region of radius $2.5'$ and background data from several boxes that sampled source-free regions of the detector. Xtend yielded a source count rate $1.295 \pm 0.003 \text{ cts s}^{-1}$ (2–10 keV) or $6.798 \pm 0.007 \text{ cts s}^{-1}$ (0.4–10 keV).

2.2. NuSTAR

NuSTAR observed NGC 4051 starting about 1 day before the *XRISM* exposures and overlapped both *XMM-Newton* exposures; see Table 1 and Figure 1. *NuSTAR* Focal Plane Mod-

ules A (FPMA) and B (FPMB) offer high signal spectral data from 3 – 60 keV for NGC 4051, facilitating determination of the primary continuum form. This yielded count rates of $0.659 \pm 0.002 \text{ cts s}^{-1}$ from FPMA and $0.640 \pm 0.002 \text{ cts s}^{-1}$ from FPMB.

2.3. XMM-Newton

XMM-Newton observed NGC 4051 over two satellite orbits, one centered on the start of the *XRISM* exposures and the second about half-way through (Figure 1). The spectra were extracted from circular regions, of radius $27''$ for the source and $45''$ for the background in Small Window mode. These were screened for periods of high background, resulting in net exposures of 80.5 ks and 85 ks for sequences 1 and 2 respectively. The corresponding net count rates are $34.10 \pm 0.02 \text{ cts s}^{-1}$ (sequence 1) and $35.28 \pm 0.02 \text{ cts s}^{-1}$ (sequence 2) from 0.3–10 keV.

Figure 1 (lower panel) compares the 2025 EPIC-pn spectrum, in νF_ν flux, with the series of 15×40 ks observations with *XMM-Newton*, taken over a month in 2009 (K. A. Pounds & S. Vaughan 2012). In 2025, NGC 4051 was

¹¹ see <https://heasarc.gsfc.nasa.gov/docs/xrism/analysis/nxb/index.html>

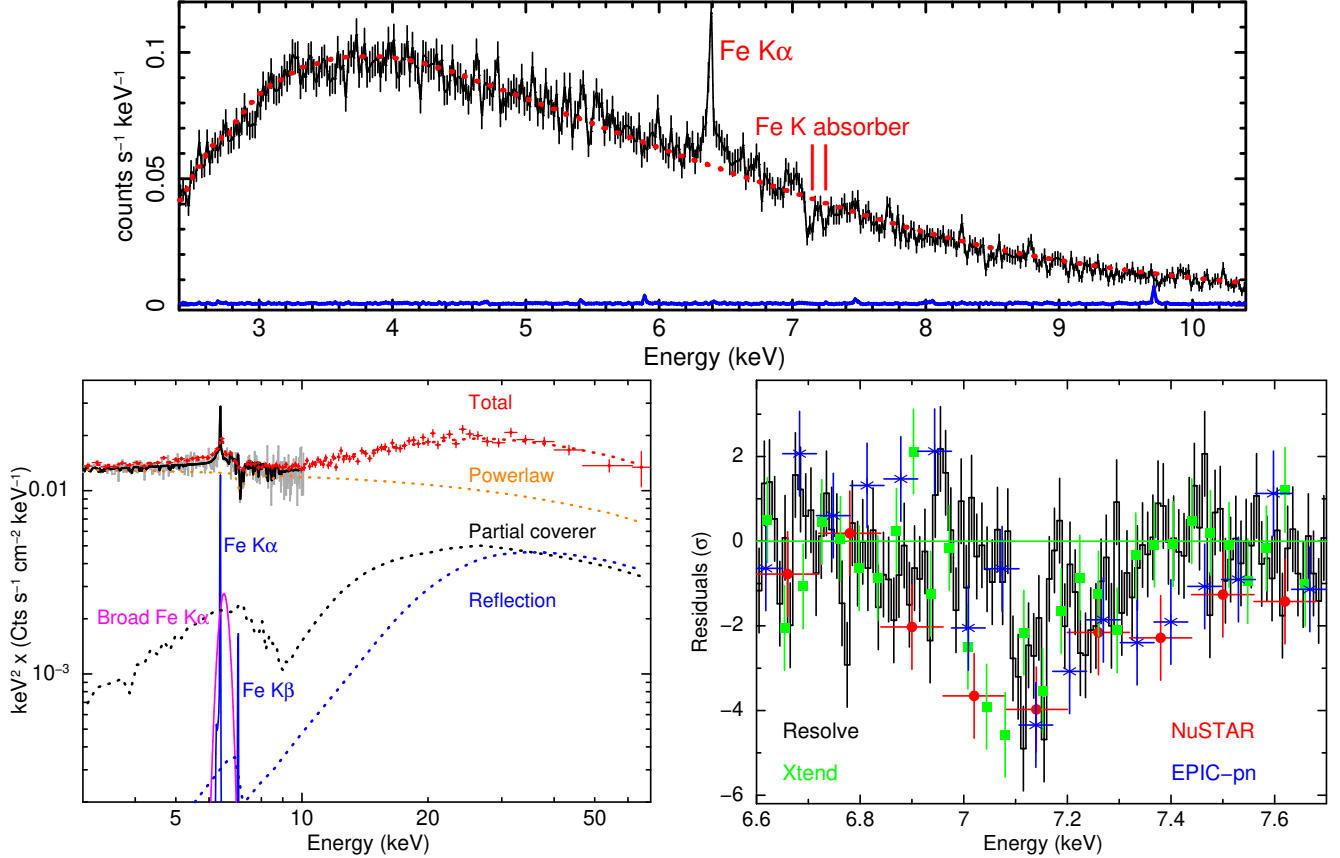


Figure 2. Time averaged spectra of NGC 4051 from the 2025 campaign. The top panel shows the *XRISM* Resolve spectrum (black), with the best-fit continuum model plotted as a red dotted line and the background (NXB) spectrum is shown in blue. The position of the strong Fe $K\alpha$ line and two absorption troughs are marked in red. The lower left plot shows the broad-band spectrum fitted with the model of Table 2. Here, Resolve is shown in black (grey errors) and *NuSTAR* FPMA in red. The individual model components (dotted lines) are as marked. The lower-right panel shows the residuals of the data to the model (in σ units), but without including any outflowing absorbers. The two absorption troughs are apparent in Resolve and appear as a single trough in the lower resolution spectra. Here, EPIC-pn (sequence 2) is also overlaid in blue and *XRISM* Xtend in green.

caught in a high flux state, at the top end of the range of 2–10 keV fluxes of $0.5 - 3.5 \times 10^{-11}$ ergs cm^{-2} s^{-1} . At lower fluxes the spectra appear harder, possibly as a result of the increased contribution of reprocessed emission, via absorption and scattering (L. Miller et al. 2010). In contrast, the 2025 observations capture a soft, bright, continuum dominated state. Note there are no strong changes in source hardness within the 2025 observations.

3. THE TIME-AVERAGED SPECTRUM

The 2 – 10 keV range of the Resolve and Xtend data were fit together with *NuSTAR* data from 3–60 keV in order to first define the time-averaged hard X-ray spectrum of NGC 4051. All models included the Galactic line-of-sight absorption, $N_{\text{H,Gal}} = 1.19 \times 10^{20} \text{cm}^{-2}$ (J. M. Dickey & F. J. Lockman 1990), via the XSPEC TBABS model (J. Wilms et al. 2000). The data were fit with the C-statistic (W. Cash 1979). The spectra were binned to 100 counts per bin, except for Resolve as noted in Section 2. Errors are quoted at 90% con-

fidence for one parameter of interest ($\Delta C = 2.71$) and all parameters are in the rest-frame at $z = 0.002336$. For the luminosity, a distance of $D = 16.6$ Mpc is adopted, using the recent Cepheid variable estimate from W. Yuan et al. (2021).

The Resolve spectrum, which captures a high flux state of NGC 4051, is shown in the upper panel of Figure 2 and shows clear deviations from a powerlaw continuum in the Fe K-shell band. Fe $K\alpha$ emission is readily apparent, including both a narrow core of the line and velocity broadened wings. A detailed description of the Fe K emission modeling will be presented in paper II.

Two absorption troughs appear to be present at energies just above 7.1 keV. These can be modeled by Gaussian absorption profiles at centroid energies of 7.14 ± 0.01 keV and 7.26 ± 0.02 keV. The energy separation of the lines is too wide to be accounted for by the H-like Fe XXVI Ly α doublet at 6.952 keV and 6.973 keV (i.e. $\Delta E = 0.021$ keV) and it is too narrow to be explained by a combination of the H-like lines and the He-like Fe XXV resonance line at 6.700 keV.

This implies that the separation of the troughs derives from two different outflow velocity components of the absorber, e.g. each trough may arise from a velocity broadened blend of the two H-like doublet lines from each absorber. Note the contribution of the neutral iron K edge at 7.112 keV is negligible, with an optical depth of $\tau < 0.02$.

The two troughs are broadened with a width of $\sigma = 25_{-4}^{+8}$ eV, which corresponds to $\sigma = 1050_{-170}^{+340}$ km s⁻¹ at 7.14 keV. Note the widths of the two troughs were consistent with each other within the errors and were kept tied in the fits. Overall, the addition of the two troughs improves the fit statistic by $\Delta C = -35.8$ and $\Delta C = -16.6$ with respect to the Resolve data for the lower and higher energy components. According to the Akaike Information Criteria (AIC, H. Akaike 1974; M. Y. J. Tan & R. Biswas 2012), the troughs are significant with null hypothesis probabilities of $P_{AIC} = 3.4 \times 10^{-7}$ and $P_{AIC} = 1.8 \times 10^{-3}$ respectively.¹²

3.1. Photoionization Modeling

In order to model the absorption troughs and the broadband spectrum between 2–60 keV, photoionization models were constructed using XSTAR (T. R. Kallman et al. 2004) and the input SED of NGC 4051 (see Appendix A). The input continuum is approximated by a photon index slightly steeper than $\Gamma = 2$, modified by an exponential cut-off (CUTOFFPOW) at hard X-rays. The absorption tables were calculated for Solar abundances (M. Asplund et al. 2021) and turbulence velocities covering the range from $v_{\text{turb}} = 100 - 2700$ km s⁻¹. The MYTORUS model (K. D. Murphy & T. Yaqoob 2009) accounts for the narrow Fe K $\alpha_{1,2}$ and K β emission lines, using the latest line tables as described in T. Yaqoob (2024) which incorporate the laboratory line profiles of G. Hölzer et al. (1997). These were then convolved with a Gaussian broadening function to describe their velocity widths. The much broader Fe K α wings are modeled by a separate Gaussian profile. A scattered MYTORUS component models the associated Compton hump.

The phenomenological form of the model is simply:-

$$\text{CONSTANT} \times \text{TBABS} \times [(2 \text{XSTAR}_{\text{Fe}} \times \text{ZXIPCF} \times \text{CUTOFFPOW}) + \text{MYTORUS}_{\text{scatt}} + \text{MYTORUS}_{\text{line}} + \text{GAUSS}].$$

Here the cut-off power-law continuum is absorbed by two outflowing photoionized absorbers (XSTAR_{Fe}). A lower ionization partial covering absorber, represented by the ZXIPCF model in XSPEC (J. N. Reeves et al. 2008), is also included, whereby a fraction (f_{cov}) of the continuum is intercepted by the absorber and the remainder ($1 - f_{\text{cov}}$) is unattenuated.

¹² The AIC is equivalent to $AIC = 2k + C_{\text{stat}}$, where k is the number of fitted parameters. The null hypothesis probability is found by the likelihood ratio test as $N = e^{\Delta AIC/2}$.

Table 2. Spectral parameters for the mean spectrum.

Parameter	Value
Cut-off Powerlaw	
Γ	2.05 ± 0.03
Normalization ^a	$2.11 \pm 0.13 \times 10^{-2}$
E_{cut}	110_{-40}^{+95} keV
MyTorus Line + Scattered	
Normalization ^a	$0.91 \pm 0.18 \times 10^{-2}$
Column Density, N_{H}	$> 6.3 \times 10^{24}$ cm ⁻²
Convolution, σ_{gauss} ^b	$2.9_{-1.8}^{+2.2}$ eV
FWHM width	320_{-200}^{+250} km s ⁻¹
Broad Iron K Line	
Broad Fe K Gaussian:-	
Energy	6.445 ± 0.025 keV
Width, σ_{gauss}	$0.101_{-0.030}^{+0.046}$ keV
FWHM width	11000_{-3300}^{+5000} km s ⁻¹
Line Flux	$1.9 \pm 0.4 \times 10^{-5}$ photons cm ⁻² s ⁻¹
Equivalent Width (EW)	52 ± 11 eV
Partial Covering Absorber	
Column Density, N_{H}	$1.14 \pm 0.11 \times 10^{24}$ cm ⁻²
Ionization, $\log \xi^c$	2.80 ± 0.06
Covering Fraction, f_{cov}	0.37 ± 0.03
Outflow Zone 1	
Column Density, N_{H}	$1.7 \pm 0.5 \times 10^{23}$ cm ⁻²
Ionization, $\log \xi^c$	$4.8_{-0.3}^{+0.2t}$
Turbulence velocity, v_{turb}	1500_{-600}^{+800} km s ^{-1t}
Outflow velocity, v/c	-0.0248 ± 0.0014 $(-7400 \pm 400 \text{ km s}^{-1})$
$\Delta C/\Delta\nu^d$	$-57.6/4$
Null probability, P_{AIC}^e	1.7×10^{-11}
Outflow Zone 2	
Column Density, N_{H}	$6.8 \pm 3.7 \times 10^{22}$ cm ⁻²
Outflow velocity, v/c	-0.040 ± 0.002 $(-12000 \pm 600 \text{ km s}^{-1})$
$\Delta C/\Delta\nu^d$	$-34.8/2$
Null probability, P_{AIC}^e	2.0×10^{-8}
Other Parameters	
C^f (NuSTAR/Resolve)	1.05 ± 0.01
C^f (Xtend/Resolve)	0.94 ± 0.01
Flux (2-10 keV)	3.5×10^{-11} ergs cm ⁻² s ⁻¹

^a Power-law flux in units of photons cm⁻² s⁻¹ keV⁻¹ at 1 keV.

^b Velocity width at 6.4 keV through Gaussian convolution.

^c Units of Ionization (ξ) are ergs cm s⁻¹.

^d Improvement in ΔC upon adding the component to the model. $\Delta\nu$ is the change in degrees of freedom.

^e Null hypothesis probability derived from the AIC statistic.

^f Multiplicative cross normalization factor.

^t The ionization and turbulence are tied between zones 1 and 2.

A constant cross normalization factor between instruments is included in front of all of the components.

The spectral parameters are listed in Table 2 and the fit to the data is plotted in Figure 2 (lower left). The overall fit statistic is $C/\nu = 5239.1/5184$. The X-ray power-law has a photon index of $\Gamma = 2.05 \pm 0.03$, with a high energy cut-off of $E_{\text{cut}} = 110_{-40}^{+95}$ keV which is typical of Seyfert galaxies observed with *NuSTAR* (R. Middei et al. 2019). The two XSTAR absorbers are both outflowing, with velocities of $v/c = -0.0248 \pm 0.0014$ and $v/c = -0.040 \pm 0.002$ which corresponds to $v_{\text{out1}} = -7400 \pm 400 \text{ km s}^{-1}$ and $v_{\text{out2}} = -12000 \pm 600 \text{ km s}^{-1}$. These velocities lie near to the boundary of the definition of an ultra fast outflow at -10000 km s^{-1} (F. Tombesi et al. 2010). No other Fe K absorption components are required.

The absorbers are highly ionized, with an ionization parameter of $\log \xi = 4.8_{-0.3}^{+0.2} \text{ erg cm s}^{-1}$. Indeed, negligible He-like absorption is apparent and the absorption arises mainly from H-like Fe. Neither absorber imparts any significant opacity in the lower energy part of the Resolve band between 2–4 keV, nor is any predicted in the soft X-ray band below 2 keV. For simplicity, we have assumed both outflowing zones have the same ionization parameter, which are otherwise consistent within errors. The high ionization parameter, along with the column densities that are observed ($N_{\text{H}} \approx 10^{23} \text{ cm}^{-2}$) are typical of UFOs in nearby AGN (F. Tombesi et al. 2010; J. Gofford et al. 2013). The turbulence velocity was found to be $v_{\text{turb}} = 1500_{-600}^{+800} \text{ km s}^{-1}$ (equivalent to $\sigma_v = 1100_{-400}^{+600} \text{ km s}^{-1}$). At this velocity width, the individual Fe XXVI components are not separated into their constituent doublet lines and each component appears as a single, velocity broadened H-like trough.

Against the full dataset, each of the outflowing zones is highly significant with $\Delta C/\Delta \nu = -57.6/4$ (slower zone) and $\Delta C/\Delta \nu = -34.8/2$ (faster zone). These correspond to null hypothesis probabilities of 1.7×10^{-11} and 2.0×10^{-8} respectively, according to the AIC. The absorbers are also independently detected across all instruments; e.g. see Figure 2 (lower right panel), which shows the residuals of the individual Resolve, Xtend and *NuSTAR* and *XMM-Newton* spectra. However, only Resolve separates the absorption into two kinematically distinct components, which appear as a single trough in the CCD resolution data.

Partial covering absorption has been claimed previously in NGC 4051, in particular to account for pronounced spectral curvature observed in lower flux observations of this AGN which display much harder, more absorbed spectra (Y. Terashima et al. 2009; L. Miller et al. 2010; A. P. Lobban et al. 2011). In this high flux observation, the effects of the partial coverer upon the spectrum are modest. While its column density is high ($N_{\text{H}} \approx 10^{24} \text{ cm}^{-2}$, Table 2), its line of sight covering fraction is very low ($f_{\text{cov}} =$

0.37 ± 0.03). As a result of its high column yet low covering, its transmission between 2–10 keV is $< 10\%$ of the direct power-law continuum (see Figure 2, left). Subsequently it imparts no detectable Fe K absorption lines nor edges upon the Resolve spectrum. Its primary effect is in modeling an additional hard X-ray excess seen in the *NuSTAR* spectrum above 10 keV, above that modeled by the MYTORUS reprocessor. The physical origin of this hard excess component will be deferred to future works.

4. TIME SLICED SPECTRAL ANALYSIS

The Resolve spectrum was then sliced into five time intervals in order to characterize the variability of the outflowing absorber. These are slice 1 (0 – 65 ks), slice 2 (65 – 130 ks), slice 3 (130 – 170 ks), slice 4 (170 – 210 ks) and slice 5 (210 – 310 ks), as marked in Figure 1. The sampling of the slices ensures there are at least 10^4 counts in each Resolve spectrum. Here, slice 4 was chosen to cover the high portion of the X-ray lightcurve, with persistent X-ray flares and which is devoid of dips, while slice 5 covers a prolonged quiescent period following this. The time sliced Resolve spectra are plotted in Figure 3, zoomed into the 6–8 keV band and are also compared to the mean spectrum.

To fit the slices, the same time-averaged model as listed in Table 2 was adopted. Asides from the continuum flux, all the parameters were fixed to the best fit values of the mean spectrum as no significant spectral variability of the continuum was found. For example, varying the photon index between the time sliced spectra did not result in any significant changes within the uncertainties; e.g. the lowest value was found in slice 3 ($\Gamma = 2.01 \pm 0.05$) and the highest value in slice 4 ($\Gamma = 2.11 \pm 0.06$), which are consistent within errors. Likewise, no change in the intensity of the narrow iron $K\alpha$ emission was found.

4.1. Gaussian Line Search

The variability of the absorption troughs was initially assessed by using single Gaussian trough in order to perform a blind trial search. This was performed for each slice, by varying the absorption line energy in 5 eV energy increments (i.e. at the resolution of Resolve) over the 6.6–9.0 keV band. The line widths were fixed to $\sigma = 20 \text{ eV}$, consistent with the measured width in the mean spectrum, although allowing the widths to vary did not alter the search parameters. The scan results are shown in Appendix B.

The resulting best-fit absorption line values from each slice are noted in Table 3. The line search revealed a single, statistically significant trough in each of the five slices, which occur over the same expected energy range of 7.1–7.3 keV as per the mean spectrum. The only exception is in slice 5, where an additional higher energy trough was also found at $> 99\%$ significance near to 8 keV. No other troughs were found to be significant at the $> 95\%$ confidence level.

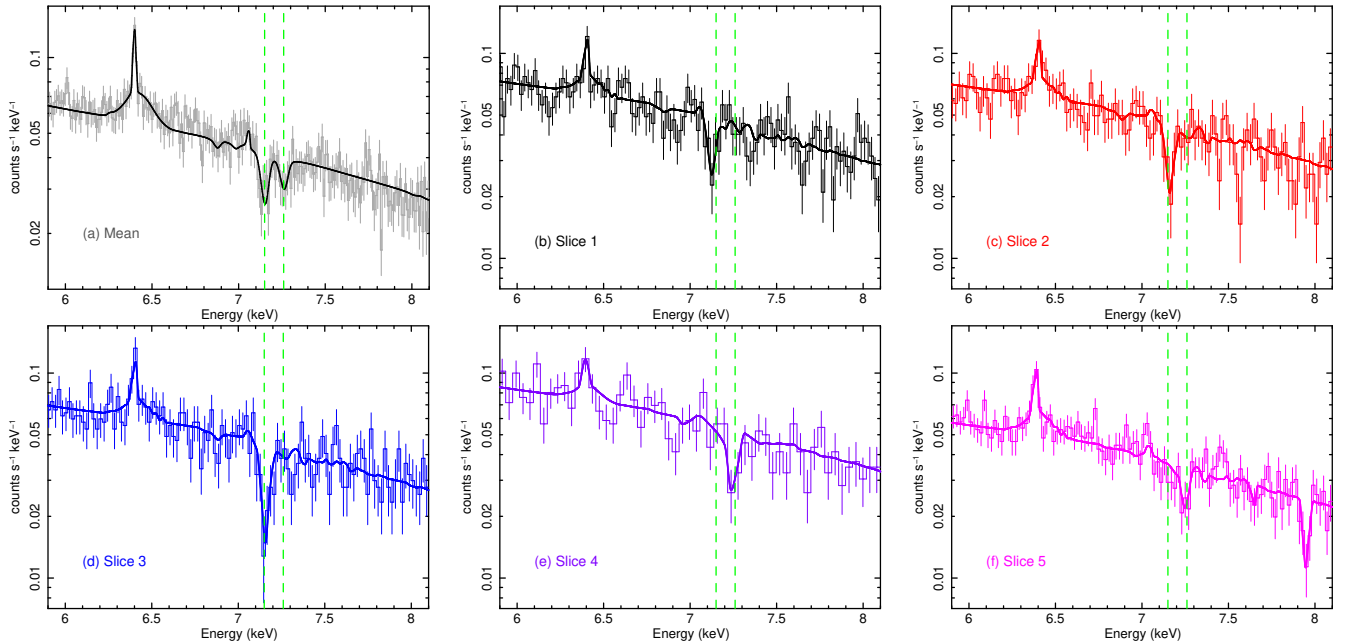


Figure 3. Time-dependent analysis of the Resolve spectrum, showing the mean spectrum (panel a) and the 5 slices (panels b–f) against the best fit absorber model as described in Table 3. The vertical dashed green lines mark the centroid energies of the two Fe K absorption troughs as measured in the mean spectrum at 7.14 keV and 7.26 keV respectively. In slices 1–3 the centroid energy of the absorption trough is consistent with the low energy trough at 7.14 keV, while in slices 4 and 5 the absorption line appears more blue-shifted coincident with the 7.26 keV trough – see Table 3 for values. This may suggest an increase in velocity in the Fe K absorber during the observation. Note slice 5 also shows a higher absorption trough at 7.96 keV, which might originate from an ultra fast outflow at a velocity of $-0.13c$.

However, the centroid energies of the troughs are variable. In the first three slices, a single absorption trough was found from 7.12 – 7.16 keV, coincident with the first absorption trough in the mean spectrum, while the second higher energy absorption trough was not found. In contrast in the last two slices 4 and 5, the centroid energy of the absorption trough shifts to 7.25 – 7.26 keV, coincident with the second absorption line in the mean spectrum and no lower energy trough is found; see Figure 3 for a comparison. Thus the sliced spectra reveal an increase in absorption line energy with time, with a significant jump appearing between slices 3 and 4. Superposition of all the individual troughs then result in the double trough seen in the average spectrum.

The two EPIC-pn exposures confirm the absorption lines. *XMM-Newton* sequence 1 covers the period from -45 ks to 33 ks (where $T = 0$ corresponds to the start of the Resolve exposure), coinciding with slice 1. Sequence 2 corresponds to the period from 130 – 210 ks, coinciding with slice 3 and 4 obtained with Resolve. While EPIC-pn cannot resolve the profile, there is some indication of an energy shift from 7.11 ± 0.05 keV to 7.22 ± 0.04 keV; see Table 3 for details. The behavior is consistent with the increase in the absorption trough energy as seen in Resolve. The same behavior is not confirmed in the Xtend spectra, although they are consistent within the larger uncertainties.

4.2. Modeling with an accelerating absorber

Informed by the above results, a single XSTAR absorber was added to the baseline spectral model to probe its variations. The absorber outflow velocity was allowed to vary, along with its column, ionization and turbulence velocity across the five slices. However the latter two parameters were found to be consistent within the errors and were subsequently fixed to a single value, with $\log \xi = 4.8^{+0.2}_{-0.3}$ for the ionization and $v_{\text{turb}} = 1340^{+660}_{-600}$ km s $^{-1}$ for the turbulence. Thus only the column density, outflow velocity and the power-law normalization were allowed to vary.

A good fit to all five slices can be obtained with this simple prescription for the variability, with $C/\nu = 1798.2/1809$ and the results are shown in Table 3. The absorber variability is driven by changes in the absorber velocity, which approximately doubles from $v/c = -0.0222 \pm 0.0021$ (-6700 ± 600 km s $^{-1}$) in slice 1, to $v/c = -0.0405 \pm 0.0022$ (-12200 ± 700 km s $^{-1}$) in slice 5. The changes in velocity, column and 2–10 keV luminosity are plotted in Figure 4 (left panels). The most pronounced change in the velocity occurs between slice 3 and 4 and coincides with the onset of the strong X-ray flaring in slice 4. In contrast, the column density is approximately constant.

Thus the wind acceleration may be the cause of the energy shift of the absorber. From a linear fit of velocity versus time across all five slices, the acceleration is then $a = 2500 \pm$

Table 3. Summary of absorption zones fitted to the time sliced spectra.

Slice	$L_{2-10 \text{ keV}}$ $10^{41} \text{ erg s}^{-1}$	Gaussian fit				XSTAR fit			
		E^a keV	EW eV	ΔC	P_{AIC}^b	$\log N_{\text{H}}$ 10^{22} cm^{-2}	v/c	ΔC	P_{AIC}^b
Resolve 1	12.7	$7.122^{+0.016}_{-0.014}$	-24^{+10}_{-9}	12	1.83×10^{-2}	$23.32^{+0.17}_{-0.24}$	-0.0222 ± 0.0021	14.6	4.99×10^{-3}
Resolve 2	12.3	$7.162^{+0.011}_{-0.013}$	-28^{+10}_{-9}	15.5	3.18×10^{-3}	$23.41^{+0.15}_{-0.21}$	-0.0271 ± 0.0015	17.8	1.01×10^{-3}
Resolve 3	12.1	7.153 ± 0.009	-37^{+9}_{-7}	26.4	1.37×10^{-5}	$23.58^{+0.14}_{-0.18}$	-0.0264 ± 0.0015	27.2	9.17×10^{-6}
Resolve 4	14.8	$7.252^{+0.013}_{-0.017}$	-34^{+13}_{-10}	13.1	1.06×10^{-2}	$23.48^{+0.19}_{-0.30}$	-0.0388 ± 0.0023	11.6	2.24×10^{-2}
Resolve 5	9.9	$7.257^{+0.014}_{-0.018}$	-24^{+12}_{-6}	13.1	1.06×10^{-2}	$23.20^{+0.16}_{-0.30}$	-0.0405 ± 0.0022	12.2	1.66×10^{-2}
		$7.963^{+0.014}_{-0.009}$	-27^{+9}_{-10}	14.8	4.52×10^{-3}	$23.32^{+0.20}_{-0.25}$	-0.1336 ± 0.0008	17.2	1.36×10^{-3}
EPIC-pn Seq 1		7.11 ± 0.05	-22 ± 9	13.7	7.8×10^{-3}	$23.26^{+0.15}_{-0.22}$	-0.020 ± 0.008	18.1	8.6×10^{-4}
EPIC-pn Seq 2		7.22 ± 0.04	-31 ± 9	28.3	5.3×10^{-6}	$23.41^{+0.13}_{-0.15}$	-0.035 ± 0.006	35.1	1.8×10^{-7}
Mean Resolve		$7.141^{+0.011}_{-0.009}$	-26 ± 6	35.8	3.38×10^{-7}	$23.23^{+0.11}_{-0.15}$	-0.0255 ± 0.0014	37	1.86×10^{-7}
		$7.263^{+0.007}_{-0.025}$	-17^{+6}_{-7}	16.6	1.84×10^{-3}	$23.00^{+0.18}_{-0.22}$	-0.0398 ± 0.0017	15.9	2.61×10^{-3}

^a For the Gaussian fits to the individual slices we adopted a line width of $\sigma = 20 \text{ eV}$. In the mean spectrum the width of the two absorption lines are tied, we measured $\sigma = 25^{+8}_{-4} \text{ eV}$.

^b Null probability of adding either the Gaussian absorption line or the XSTAR absorber, calculated via the AIC statistic.

400 cm s^{-2} . This assumes a constant acceleration, however a more rapid increase in velocity occurs from slice 3 to 4. From comparing the midpoints of these slices, this yields $a = 9300 \pm 2100 \text{ cm s}^{-2}$. Thus the acceleration covers a likely range from $2.5 - 10.0 \times 10^3 \text{ cm s}^{-2}$, equivalent to $2.5 - 10g$ at the Earth's surface.

The null hypothesis scenario where the absorption is not variable was also tested. If first the column density is fixed to a constant value across all of the slices, then the fit statistic is very similar ($C/\nu = 1804.3/1813$), as expected if the opacity remains similar through the observation. On the other hand, if the velocity is also held constant, then the fit statistic is significantly worse, with $C/\nu = 1844.9/1817$. The change in the fit statistic is then $\Delta C/\Delta\nu = -40.6/4$, equivalent to $\Delta\text{AIC} = -32.6$ and a null probability of $P_{\text{AIC}} = 8.3 \times 10^{-8}$.

As is noted in Section 4.1, slice 5 appears to show a higher energy absorption trough centered just below 8 keV . Adding in an additional XSTAR absorber to model this trough results in a much higher outflow velocity of $v/c = -0.1336 \pm 0.008$ (see Table 3). While the additional of this high velocity is formally significant, with $P_{\text{AIC}} = 1.4 \times 10^{-3}$, we caution that it occurs only in the final lower flux slice and not in the mean spectrum. In contrast, the lower velocity zones appear in all the slices as well as in the mean spectrum. However, its velocity is consistent with previous measurements of a faster UFO with *XMM-Newton* (K. A. Pounds & S. Vaughan 2012).

4.3. Modeling with two transiting absorbers

Alternatively, instead of one accelerating outflow, the Fe K absorption may arise from two independent absorption zones of different velocities which transit across the X-ray source at different times. To test this hypothesis, two XSTAR absorbers were added, allowing the column of each zone to vary across all 5 slices. In this scenario, the absorber velocities were restricted to a narrow range, with $v/c = -0.025 \pm 0.005$ for zone 1 and $v/c = -0.040 \pm 0.005$ for zone 2, such that the varying profiles cannot be accounted for by large velocity variations. An equally good fit was obtained with this model set-up, with $C/\nu = 1795.8/1804$. The resulting column density variations of the two zones is plotted in Figure 4 (right panels) and are listed in Table 4.

In the two zone scenario, the lowest velocity ($-0.025c$) absorber dominates the Fe K band opacity in slices 1–3, while it is not detected in slices 4 and 5. The converse is the case for the faster $-0.04c$ zone, which it is not present during slices 1–3 but is detected in slices 4 and 5. Here the two absorbers are likely to be different outflowing streamlines or clouds, which cross the X-ray source during different portions of the observations at an approximately constant velocity but with varying columns.

5. DISCUSSION

High resolution X-ray spectroscopy of Fe K outflows in AGN with *XRISM* is revealing a wealth of outflow components in unprecedented detail. The emerging picture is that AGN outflows are structured, clumpy, cover a wide range of velocities and can sometimes be time vari-

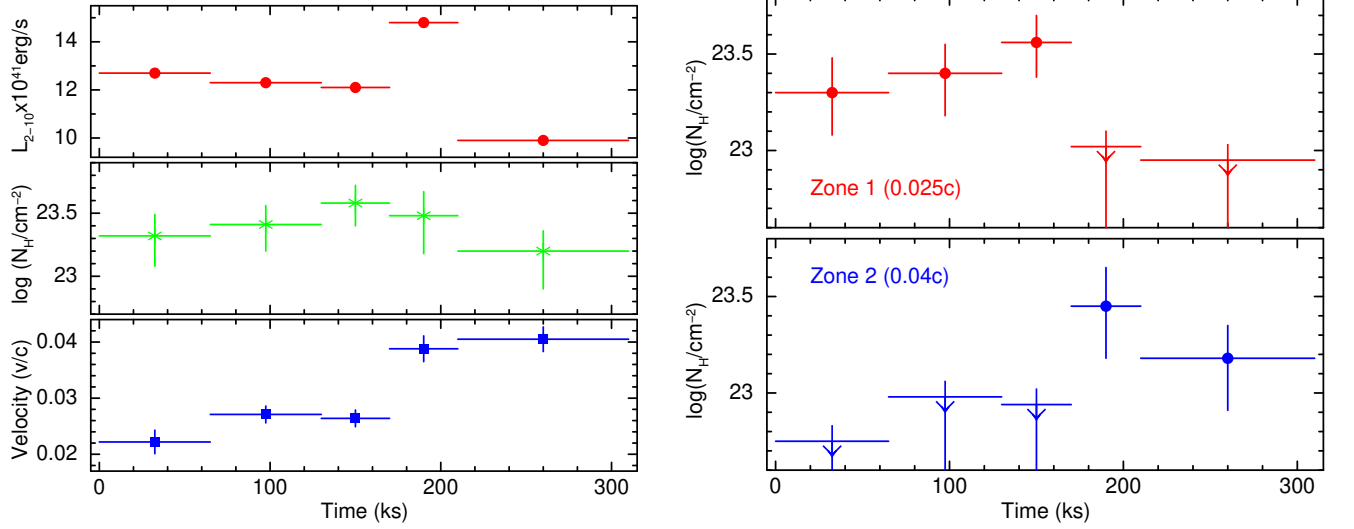


Figure 4. Results from fitting the Resolve slices. The left plot shows the results from fitting a single absorption zone, allowing the outflow velocity to vary. The top panel shows the 2–10 keV luminosity, the middle panel the column density and the lower panel the outflow velocity. The absorber velocity increases through the observation, with a sharp jump occurring between slices 3 and 4. The right plot shows the case of fitting two separate absorbers to the slices, where the velocity is restricted to $v/c = -0.025 \pm 0.005$ and $v/c = -0.040 \pm 0.005$ for each zone. Here, changes in the column density of the two zones accounts for the variability. Thus the slower zone is apparent during the first 3 slices and is not detected in slices 4 and 5. Conversely, the faster absorber is only apparent in slices 4 and 5, with upper-limits only during slices 1–3.

Table 4. Column Density Variations for Two Transiting Absorbers

Slice	Zone 1 ^a	Zone 2 ^b
	$\log(N_{\text{H}}/\text{cm}^{-2})$	$\log(N_{\text{H}}/\text{cm}^{-2})$
1	$23.3^{+0.18}_{-0.22}$	< 22.85
2	$23.4^{+0.15}_{-0.22}$	< 23.08
3	$23.56^{+0.14}_{-0.18}$	< 23.04
4	< 23.12	$23.45^{+0.20}_{-0.27}$
5	< 23.04	$23.18^{+0.17}_{-0.27}$

^aZone 1, $v/c = -0.025 \pm 0.005$

^bZone 2, $v/c = -0.040 \pm 0.005$

able (XRISM Collaboration et al. 2025; M. Mehdipour et al. 2025; H. Noda et al. 2025; M. Mizumoto et al. 2026; X. Xiang et al. 2025; A. Juráňová et al. 2025; L. Gu et al. 2025; L. W. Brenneman et al. 2025; F. Zaidouni et al. 2026).

The XRISM Resolve spectrum of NGC 4051, which occurred in a high flux state, has revealed at least two variable Fe K absorbers with velocities of 0.025c and 0.040c. A transient detection of an even faster 0.13c zone appears at the end of the observation (slice 5). The main Fe K absorption variability is manifested by an increase in velocity from 0.02 – 0.04c over a 300 ks timescale. There are two possible origins for the velocity increase; either, (i) through the separate transits of two absorbers of different velocities or, (ii)

through direct acceleration of the outflow in a single streamline. Both scenarios can provide an equally good fit to the data and are discussed below.

5.1. Transiting absorber scenario

In the transiting case, the slower (0.025c) absorber crosses the AGN during slices 1–3 (0–170 ks) and the faster outflow (0.04c) follows during slices 4–5 (170–310 ks). The crossing timescale of the transiting absorbers is $\Delta t \approx 150$ ks. The corresponding absorber size is $\Delta R = v_{\text{trans}} \Delta t$, where the transverse velocity can be set to the Keplerian velocity as $v_{\text{trans}} = (GM/R)^{1/2}$ and M is the black hole mass. Furthermore, the column density, number density n and absorber size are related as $N_{\text{H}} = n \Delta R$, while the ionization parameter is defined $\xi = L_{\text{ion}}/nR^2$, where L_{ion} is the 1–1000 Rydberg ionizing luminosity.

Combining these equations leads to an expression for the radial distance of the transiting absorber:-

$$R^{5/2} = \frac{L_{\text{ion}}}{N_{\text{H}} \xi} (GM)^{1/2} \Delta t. \quad (1)$$

From the spectral fits (Tables 2 and 3), $N_{\text{H}} = 2 \times 10^{23} \text{ cm}^{-2}$, $\log \xi = 4.8$ and from the SED, $L_{\text{ion}} \approx 10^{43} \text{ erg s}^{-1}$. For NGC 4051, the black hole mass is $\approx 10^6 M_{\odot}$ (K. D. Denney et al. 2009; M. M. Fausnaugh et al. 2017). Thus for a transit timescale of $\Delta t = 150$ ks, then the radial location of the outflowing gas is $R \approx 3 \times 10^{14} \text{ cm} \approx 10^3 R_{\text{s}}$ (R_{s} is the Schwarzschild radius) or equivalently ~ 0.1 light-days. The Keplerian transit speed is then $v_{\text{trans}} \approx 10^4 \text{ km s}^{-1}$.

This distance estimate is an order of magnitude inside the inferred broad line region (BLR) radius in NGC 4051, of 1.9 ± 0.5 light-days (K. D. Denney et al. 2009) and is well inside its dust sublimation radius of 0.01 pc (Y. Krongold et al. 2007). The distance is consistent with the time lags of the hard X-ray reprocessor in archival *NuSTAR* data, of a few thousand seconds (T. J. Turner et al. 2017).

Thus the Fe K absorbers are likely to be located within the optical BLR and could originate from an accretion disk wind (D. Proga & T. R. Kallman 2004). At this distance and from the above expressions, then the gas density is $n = 2 \times 10^9 \text{ cm}^{-3}$ and the absorber size-scale is $\Delta R \approx 10^{14} \text{ cm}$, which is of the order of its radial distance. At $R \approx 10^3 R_s$, the escape speed is $0.03c$, similar to the outflow velocities of the absorbers. In this context, the faster ($0.13c$) zone may arise from closer in, where its escape radius is at $\approx 50 R_s$.

5.2. Constraints on an accelerating outflow

As the absorber column density remains approximately constant through the observation (Table 3 and Figure 4), this might suggest a single, accelerating outflow. Here, the assumption of a Keplerian transit velocity can be relaxed and the velocity variations instead derive from the in-situ acceleration of the gas. However, the absorber size-scale should be similar to (or larger) than the size of the X-ray corona, in order for the absorbing gas to fully cover the continuum emission. If the absorber is too compact with a low line-of-sight covering fraction, then the absorption profiles will become too weak to be detectable.

An estimate of the X-ray coronal size derives from the flux doubling time, which is $\Delta t \sim 1 \text{ ks}$ from the Xtend light-curve in Figure 1. From the light crossing time, the coronal size is inferred to be $D_{\text{cor}} = c\Delta t = 3 \times 10^{13} \text{ cm}$ (or $D \sim 100 R_s$). Assuming the absorber fully covers the continuum source, then the absorber size $D_{\text{abs}} \approx D_{\text{cor}}$. The absorber density is then $n = \frac{N_{\text{H}}}{D_{\text{abs}}} \sim 6 \times 10^9 \text{ cm}^{-3}$. The radial distance of the absorber inferred from the ionization parameter is then $R \approx 2 \times 10^{14} \text{ cm}$. Note that the maximum possible absorber distance derives from the condition that its size is of the order of its radial distance (i.e. $\Delta R/R \approx 1$), which is then $R \lesssim L_{\text{ion}}/N_{\text{H}}\xi \approx 10^{15} \text{ cm}$ (D. M. Crenshaw et al. 2003).

The gas acceleration may be caused by radiation pressure. As the Fe K absorber is highly ionized, arising from mainly H-like iron with a negligible force multiplier (R. C. Dannen et al. 2019), then the pressure is imparted through electron scattering. The radiation pressure is simply:-

$$F_{\text{rad}} = \frac{L_{\text{bol}}}{4\pi R^2 c} \sigma_{\text{T}} N_{\text{H}}, \quad (2)$$

where σ_{T} is the Thomson cross-section and L_{bol} is the bolometric luminosity. Dividing by mass per unit area ($\mu m_{\text{p}} N_{\text{H}}$) gives the acceleration:-

$$a = \frac{L_{\text{bol}}}{4\pi R^2 c} \frac{\sigma_{\text{T}}}{\mu m_{\text{p}}}, \quad (3)$$

where $\mu \approx 1.4$ is the average atomic mass. From the NGC 4051 SED (see Appendix), $L_{\text{bol}} \sim 3 \times 10^{43} \text{ erg s}^{-1}$, which is about 25% of the Eddington luminosity for a black hole mass of $M_{\text{BH}} = 10^6 M_{\odot}$. Taking the lower of the radial estimates, of $R = 2 \times 10^{14} \text{ cm}$, then yields $a \approx 500 \text{ cm s}^{-2}$. This is insufficient by about an order of magnitude to drive the gas in NGC 4051, compared to the observed acceleration in Section 4.2 of $a \approx 2.5 - 10 \times 10^3 \text{ cm s}^{-2}$. To achieve this, the luminosity would have to be at least $\times 10$ greater than observed, pushing NGC 4051 above the Eddington limit. Alternatively the gas could be located further in, closer to $100 R_s$, but this is problematic as it is well inside the escape radius for gas with a terminal velocity of $0.04c$.

5.3. An MHD driven wind

Instead, MHD driving (R. D. Blandford & D. G. Payne 1982; K. Fukumura et al. 2010) may explain the variable wind in NGC 4051. This can be powered by magnetic reconnection events (T. Di Matteo 1998), as is favored to explain the accelerating UFO in NGC 3783 (L. Gu et al. 2025) and could coincide with X-ray coronal flares.

In MHD winds, the outflow velocity can be equivalent to the Alfvén speed (V_a), which is proportion to the magnetic field strength (B) in c.g.s units as:-

$$V_a = \sqrt{\frac{B^2}{4\pi\rho}}, \quad (4)$$

where ρ is the mass density. From the above estimates for n , then $\rho \approx 10^{-14} \text{ g cm}^{-3}$ and hence for $v = 0.04c$, $B \approx 400 \text{ Gauss}$. Note for a standard disk prescription (N. I. Shakura & R. A. Sunyaev 1973), then a plausible upper bound is $B \lesssim 10^3 \text{ Gauss}$, at a distance of $10^3 R_s$ and scaled to the black hole mass of NGC 4051.

As a consistency check, we can compare the magnetic energy density (equivalent to pressure), U_B , to the gravitational energy density, U_G . At a distance of $R \approx 10^3 R_s = 3 \times 10^{14} \text{ cm}$, then $U_G = GM\rho/r \approx 4 \times 10^3 \text{ erg cm}^{-3}$. For $B = 400 \text{ Gauss}$, then $U_B = B^2/8\pi \approx 6 \times 10^3 \text{ erg cm}^{-3}$ which is of a similar order (or slightly higher). In comparison, the radiation pressure is at least an order of magnitude smaller than U_B , where per unit area $F_{\text{rad}} \approx 10^2 \text{ erg cm}^{-3}$ from equation 2. Hence a Compton (electron scattering) driven wind would be unlikely to escape. Thus MHD mechanisms may be more plausible to drive the wind in NGC 4051.

5.4. Wind Energetics

The mass outflow rate can be expressed as:-

$$\dot{M}_{\text{out}} = 4\pi bnR^2 v_{\text{out}} \mu m_{\text{p}}, \quad (5)$$

where b is a geometrical factor which is a product of the global covering factor ($f_{\text{cov}} = \Omega/4\pi$) and the volume filling factor f_{vol} ; e.g. see Y. Krongold et al. (2007); F. Tombesi et al. (2013); J. Gofford et al. (2015). Here $nR^2 = L_{\text{ion}}/\xi = 10^{38} \text{ cm}^{-1}$ in NGC 4051, $v_{\text{out}} = 10^4 \text{ km s}^{-1}$ and $\mu = 1.4$, which yields $\dot{M}_{\text{out}} = 0.05b M_{\odot} \text{ yr}^{-1}$. Nominally for $b = 1$ and an accretion efficiency of $\eta = 0.06$, this is at the Eddington accretion rate for NGC 4051, but is likely lower as $b < 1$. For example, if $f_{\text{cov}} \approx 0.4$ from the frequency of occurrence of UFOs (F. Tombesi et al. 2010), while $f_{\text{vol}} \approx \Delta R/R \approx 0.3$ from the above constraints on ΔR and R from the absorber variability, then \dot{M}_{out} is about 10% of Eddington.

The corresponding kinetic power is $L_{\text{k}} = \frac{1}{2} \dot{M}_{\text{out}} v_{\text{out}}^2 \approx b \times 10^{42} \text{ erg s}^{-1}$, which even for $b = 1$ is only 1% of Eddington in NGC 4051, with a mass of $10^6 M_{\odot}$. Overall the outflow kinetic power in this low luminosity AGN is much lower than those inferred from *XRISM* observations of more powerful, massive quasars, e.g. PDS 456 (XRISM Collaboration et al. 2025), PG 1211+143, (M. Mizumoto et al. 2026), IRAS 05189–2524 (H. Noda et al. 2025), which can reach the Eddington limit.

6. CONCLUSIONS

XRISM observed the nearby, low mass NLS1, NGC 4051, at an historically high X-ray flux. The time-averaged Resolve spectrum reveals two blue-shifted absorption troughs in the Fe K band, associated with H-like iron, with outflow velocities of 0.025c and 0.040c. Overall, the wind power is sub-Eddington. However the outflow components vary through

the observation, where the slower component is prevalent in the first part of the observation, while the higher velocity absorber is present during the latter half. The velocity variations can equally be interpreted in terms of two independent transiting absorbers, or through an accelerating absorber. In either case, the increase in velocity coincides with the brightest, flaring portion of the observation. Radiation alone, via electron scattering, appears insufficient to accelerate the gas up to 0.04c. Thus MHD mechanisms are favored to drive the wind, which may be connected to increased periods of magnetic activity in the accretion disk corona. Given its pronounced variability on short timescales, future, long *XRISM* observations of NGC 4051 would be ideal for testing the wind variability and how it responds to the continuum.

7. ACKNOWLEDGEMENTS

JR and VB acknowledge support through NASA grants 80NSSC25K7845 and 80NSSC22K0474. TJT acknowledges support from NASA Grant 80NSSC25K0493. This work was also supported by the Japan Society for the Promotion of Science (JSPS) KAKENHI grant number 24K17104 (S.O.). ATF was supported by an appointment to the NASA Postdoctoral Program at the NASA Goddard Space Flight Center, administered by Oak Ridge Associated Universities under contract with NASA. The *XRISM* observation was supported by observations with *NuSTAR* and *XMM-Newton*. The latter is an ESA science mission with instruments and contributions directly funded by ESA Member States and NASA.

AUTHOR CONTRIBUTIONS

JNR was responsible for writing and submitting the manuscript. JNR, SO, TJT, VB, SY, ATF have worked on the data reduction and analysis. TJT and SO are the PIs of the *XRISM* observation. All other authors contributed to the discussion and a review of the manuscript.

Facility: XRISM, XMM-Newton, NuSTAR

Software: HEASoft/FTOOLS, XMMSAS

APPENDIX

A. SED MODELLING

The SED was modeled using the simultaneous EPIC-pn, optical monitor (OM), and *NuSTAR* data. The OM was performed with the U filter and was corrected for Galactic reddening of $E(B - V) = 0.013$. For a phenomenological description, a broken power-law continuum was used, with a break energy fixed at 25 eV, with the lower energy portion connecting to the U band; here $\Gamma = 1.90 \pm 0.05$ below 25 eV and $\Gamma = 2.16 \pm 0.02$ above this. The emission and absorption components described in the paper were also included, as well as a soft band warm absorber which will be described in future work. A Comptonized disk blackbody function (L. Titarchuk 1994) accounts for the soft excess below 2 keV, of electron temperature $kT = 114 \pm 2 \text{ eV}$. The results are shown in Figure A1, where the left panel shows the SED spectral fit and the right panel (red points) the model corrected for line-of-sight absorption. The ionizing 1–1000 Rydberg luminosity of NGC 4051 from this model is $L_{\text{ion}} = 1.05 \pm 0.15 \times 10^{43} \text{ erg s}^{-1}$. These values are similar to those found in S. Laha et al. (2014).

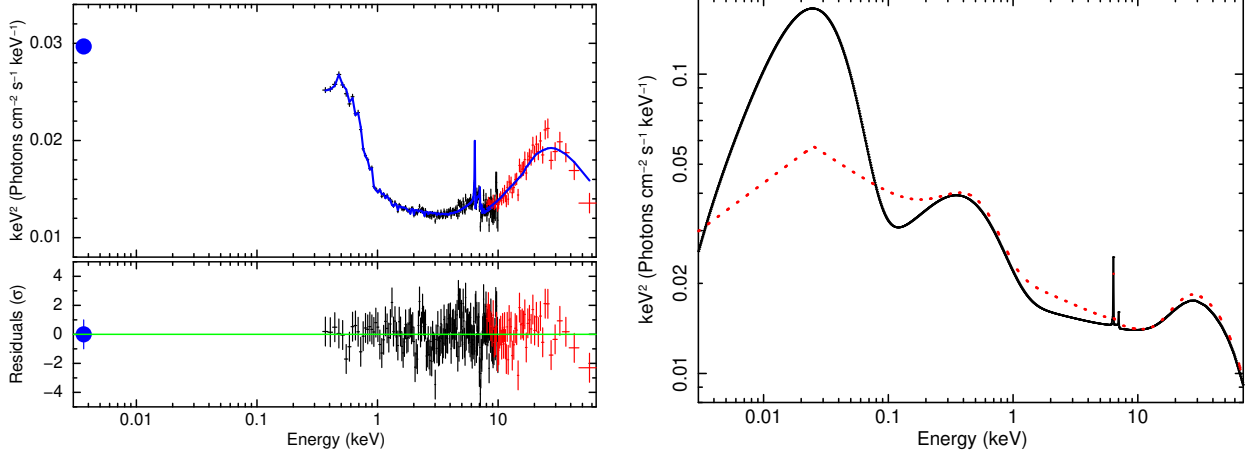


Figure A1. Results from fitting the SED. The left plot shows the fit to the data, where EPIC-pn is black, *NuSTAR* is red and the OM (U-band) point is a blue circle. The model fitted is the simple broken-powerlaw form of the SED, as described in the text. The right panel shows the comparison between the broken-powerlaw SED model (red dotted points), versus a physically motivated model computed with AGNSED (black). In the latter, the bolometric luminosity is $L_{\text{bol}} = 3 \times 10^{43} \text{ erg s}^{-1}$. The models are corrected for reddening and line-of-sight absorption.

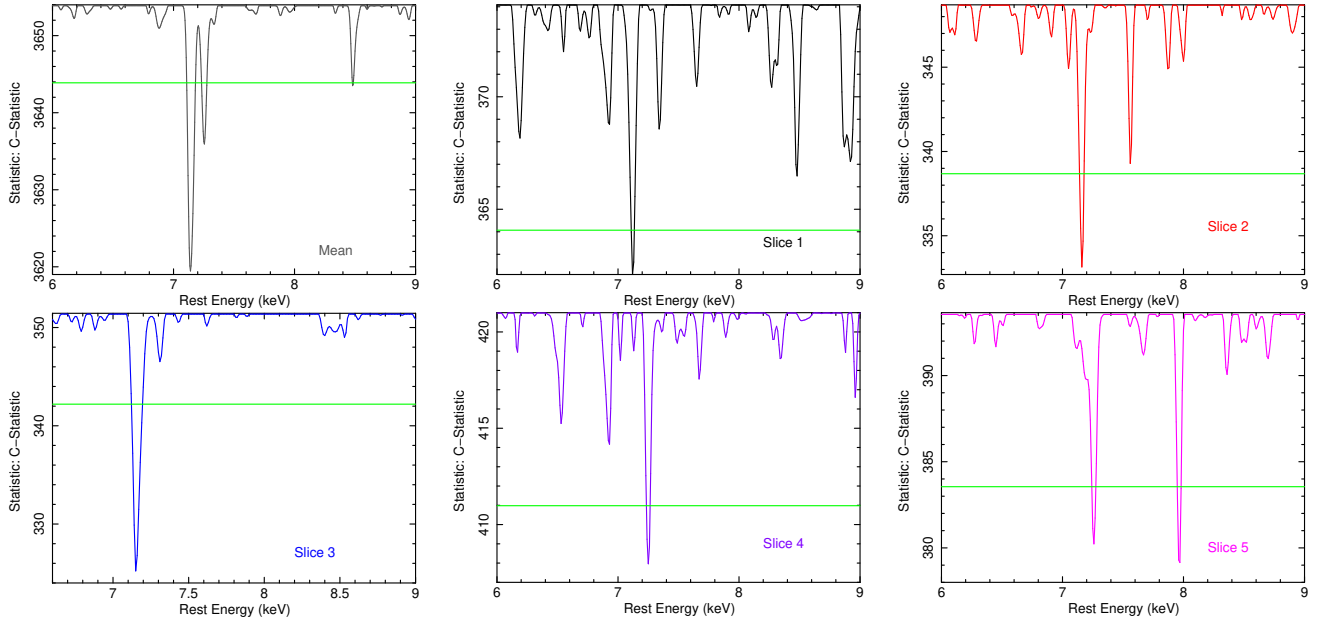


Figure B2. Results of the Gaussian absorption scans lines to the Resolve spectrum, showing the improvement in fit statistic ΔC against energy. Panel (a) shows the mean spectrum and panels b–f shows the five time-sliced spectra. The horizontal green line corresponds to a 95% AIC significance detection threshold (or $\Delta C = 10$).

For comparison, the physically motivated SED model, AGNSED within XSPEC (A. Kubota & C. Done 2018) is shown in black in the right panel of Figure A1. The model self-consistently predicts the UV bump emission from the disk (Figure A1, right), as well as the warm and hot Comptonized components; see A. Kubota & C. Done (2018) for details. For an input black hole mass of $10^6 M_{\odot}$, the accretion rate was determined to be $\log(M/\dot{M}_{\text{Edd}}) = -0.56 \pm 0.06$, or an Eddington ratio of $L/L_{\text{Edd}} = 0.27 \pm 0.03$. The predicted bolometric luminosity is then $L_{\text{bol}} = 3.4 \pm 0.4 \times 10^{43} \text{ ergs s}^{-1}$.

B. ABSORPTION LINE SCANS

As is described in Section 4.1, scans for Gaussian absorption lines, in ΔC space versus energy, were run on the Resolve spectral slices between 6.0-9.0 keV. The results are shown in Figure B1 and listed in Table 3. Significant absorption lines are present in

all five slices, detected between 7.1–7.3 keV as per the mean spectrum. At higher energies, only the trough near to 8 keV in slice 5 appears significant at > 95% confidence. No other lines are significant.

REFERENCES

- Akaike, H. 1974, *IEEE Transactions on Automatic Control*, 19, 716. doi:10.1109/TAC.1974.1100705
- Asplund, M., Amarsi, A. M., & Grevesse, N. 2021, *A&A*, 653, A141. doi:10.1051/0004-6361/202140445
- Blandford, R. D. & Payne, D. G. 1982, *MNRAS*, 199, 883. doi:10.1093/mnras/199.4.883
- Blustin, A. J., Page, M. J., Fuerst, S. V., et al. 2005, *A&A*, 431, 111. doi:10.1051/0004-6361:20041775
- Brenneman, L. W., Wilkins, D. R., Ogorzałek, A., et al. 2025, *ApJ*, 995, 2, 200. doi:10.3847/1538-4357/ae1225
- Cash, W. 1979, *ApJ*, 228, 939. doi:10.1086/156922
- Chartas, G., Brandt, W. N., & Gallagher, S. C. 2003, *ApJ*, 595, 1, 85. doi:10.1086/377299
- Chartas, G., Brandt, W. N., Gallagher, S. C., et al. 2002, *ApJ*, 579, 1, 169. doi:10.1086/342744
- Crenshaw, D. M., Kraemer, S. B., & George, I. M. 2003, *ARA&A*, 41, 117. doi:10.1146/annurev.astro.41.082801.100328
- Dannen, R. C., Proga, D., Kallman, T. R., et al. 2019, *ApJ*, 882, 2, 99. doi:10.3847/1538-4357/ab340b
- Denney, K. D., Watson, L. C., Peterson, B. M., et al. 2009, *ApJ*, 702, 2, 1353. doi:10.1088/0004-637X/702/2/1353
- Dickey, J. M. & Lockman, F. J. 1990, *ARA&A*, 28, 215. doi:10.1146/annurev.aa.28.090190.001243
- Di Matteo, T. 1998, *MNRAS*, 299, 1, L15. doi:10.1046/j.1365-8711.1998.01950.x
- Fausnaugh, M. M., Grier, C. J., Bentz, M. C., et al. 2017, *ApJ*, 840, 2, 97. doi:10.3847/1538-4357/aa6d52
- Fukumura, K., Kazanas, D., Contopoulos, I., et al. 2010, *ApJL*, 723, 2, L228. doi:10.1088/2041-8205/723/2/L228
- Gu, L., Fukumura, K., Kaastra, J., et al. 2025, *A&A*, 704, A146. doi:10.1051/0004-6361/202557189
- Gofford, J., Reeves, J. N., McLaughlin, D. E., et al. 2015, *MNRAS*, 451, 4, 4169. doi:10.1093/mnras/stv1207
- Gofford, J., Reeves, J. N., Tombesi, F., et al. 2013, *MNRAS*, 430, 1, 60. doi:10.1093/mnras/sts481
- Hölzer, G., Fritsch, M., Deutsch, M., et al. 1997, *PhRvA*, 56, 6, 4554. doi:10.1103/PhysRevA.56.4554
- Hopkins, P. F., Torrey, P., Faucher-Giguère, C.-A., et al. 2016, *MNRAS*, 458, 1, 816. doi:10.1093/mnras/stw289
- Juráňová, A., Kara, E., Behar, E., et al. 2025, *ApJ*, submitted, arXiv:2512.07950. doi:10.48550/arXiv.2512.0795
- Kallman, T. R., Palmeri, P., Bautista, M. A., et al. 2004, *ApJS*, 155, 2, 675. doi:10.1086/424039
- King, A. R. 2010, *MNRAS*, 402, 3, 1516. doi:10.1111/j.1365-2966.2009.16013.x
- King, A. 2003, *ApJL*, 596, 1, L27. doi:10.1086/379143
- Krongold, Y., Nicastro, F., Elvis, M., et al. 2007, *ApJ*, 659, 2, 1022. doi:10.1086/512476
- Kubota, A. & Done, C. 2018, *MNRAS*, 480, 1, 1247. doi:10.1093/mnras/sty1890
- Laha, S., Reynolds, C. S., Reeves, J., et al. 2021, *Nature Astronomy*, 5, 13. doi:10.1038/s41550-020-01255-2
- Laha, S., Guainazzi, M., Dewangan, G. C., et al. 2014, *MNRAS*, 441, 3, 2613. doi:10.1093/mnras/stu669
- Laurenti, M., Tombesi, F., Condò, P., et al. 2025, *A&A*, accepted, arXiv:2512.06077
- Lobban, A. P., Reeves, J. N., Miller, L., et al. 2011, *MNRAS*, 414, 3, 1965. doi:10.1111/j.1365-2966.2011.18513.x
- Matzeu, G. A., Brusa, M., Lanzuisi, G., et al. 2023, *A&A*, 670, A182. doi:10.1051/0004-6361/202245036
- Mehdipour, M., Kaastra, J. S., Eckart, M. E., et al. 2025, *A&A*, 699, A228. doi:10.1051/0004-6361/202555623
- Middei, R., Bianchi, S., Marinucci, A., et al. 2019, *A&A*, 630, A131. doi:10.1051/0004-6361/201935881
- Mizumoto, M., Reeves, J. N., Braitto, V., et al. 2026, *ApJ*, 997, 2, 219. doi:10.3847/1538-4357/ae2853
- Miller, L., Turner, T. J., Reeves, J. N., et al. 2010, *MNRAS*, 403, 1, 196. doi:10.1111/j.1365-2966.2009.16149.x
- Murphy, K. D. & Yaqoob, T. 2009, *MNRAS*, 397, 3, 1549. doi:10.1111/j.1365-2966.2009.15025.x
- Nardini, E., Reeves, J. N., Gofford, J., et al. 2015, *Science*, 347, 6224, 860. doi:10.1126/science.1259202
- Noda, H., Yamada, S., Ogawa, S., et al. 2025, *ApJL*, 993, 2, L53. doi:10.3847/2041-8213/ae14e8
- Pounds, K. A., Reeves, J. N., King, A. R., et al. 2003, *MNRAS*, 345, 3, 705. doi:10.1046/j.1365-8711.2003.07006.x
- Pounds, K. A., Reeves, J. N., King, A. R., et al. 2004, *MNRAS*, 350, 1, 10. doi:10.1111/j.1365-2966.2004.07639.x
- Pounds, K. A. & Vaughan, S. 2012, *MNRAS*, 423, 1, 165. doi:10.1111/j.1365-2966.2012.20753.x
- Proga, D. & Kallman, T. R. 2004, *ApJ*, 616, 2, 688. doi:10.1086/425117
- Reeves, J., Done, C., Pounds, K., et al. 2008, *MNRAS*, 385, 1, L108. doi:10.1111/j.1745-3933.2008.00443.x
- Reeves, J. N., O'Brien, P. T., & Ward, M. J. 2003, *ApJL*, 593, 2, L65. doi:10.1086/378218
- Serafinelli, R., Nicastro, F., Luminari, A., et al. 2025, *ApJ*, 995, 1, 6. doi:10.3847/1538-4357/ae1614
- Shakura, N. I. & Sunyaev, R. A. 1973, *A&A*, 24, 337.

- Tan, M. Y. J. & Biswas, R. 2012, MNRAS, 419, 4, 3292.
doi:10.1111/j.1365-2966.2011.19969.x
- Tashiro, M., Kelley, R., Watanabe, S., et al. 2025, PASJ, 77, S1.
doi:10.1093/pasj/psaf023
- Titarchuk, L. 1994, ApJ, 434, 570. doi:10.1086/174760
- Terashima, Y., Gallo, L. C., Inoue, H., et al. 2009, PASJ, 61, S299.
doi:10.1093/pasj/61.sp1.S299
- Tombesi, F., Cappi, M., Reeves, J. N., et al. 2013, MNRAS, 430, 2,
1102. doi:10.1093/mnras/sts692
- Tombesi, F., Cappi, M., Reeves, J. N., et al. 2010, A&A, 521, A57.
doi:10.1051/0004-6361/200913440
- Turner, T. J., Miller, L., Reeves, J. N., et al. 2017, MNRAS, 467, 4,
3924. doi:10.1093/mnras/stx388
- Wilms, J., Allen, A., & McCray, R. 2000, ApJ, 542, 2, 914.
doi:10.1086/317016
- Xiang, X., Miller, J. M., Behar, E., et al. 2025, ApJL, 988, 2, L54.
doi:10.3847/2041-8213/adee9b
- Xrism Collaboration, Audard, M., Awaki, H., et al. 2025, Nature,
641, 8065, 1132. doi:10.1038/s41586-025-08968-2
- Yamada, S., Kawamuro, T., Mizumoto, M., et al. 2024, ApJS, 274,
1, 8. doi:10.3847/1538-4365/ad5961
- Yaqoob, T. 2024, MNRAS, 527, 1, 1093.
doi:10.1093/mnras/stad3257
- Yuan, W., Macri, L. M., Peterson, B. M., et al. 2021, ApJ, 913, 1,
3. doi:10.3847/1538-4357/abf24a
- Zaidouni, F., Kara, E., Kosec, P., et al. 2026, , arXiv:2601.00795.